Highlights

WlCount: Geological lamination detection and counting using an image analysis approach

NON PEER-REVIEWED PREPRINT

Fabio Oriani, Pauline C. Treble, Andy Baker, Gregoire Mariethoz

- A new technique for laminae or tree-ring detection and counting
- Dynamic Time Warping used to extract laminae time series from entire 2D images
- A GUI allows the user operating a semi-automatic count with no parameter setup
- The technique is adaptive to complex and weakly defined laminated structures

WlCount: Geological lamination detection and counting using an image analysis approach

NON PEER-REVIEWED PREPRINT

Fabio Oriani[a], Pauline C. Treble[b,c], Andy Baker[c] and Gregoire Mariethoz[a]

[a] *Institute of Earth Surface Dynamics (IDYST), University of Lausanne, Lausanne, Switzerland*
[b] *ANSTO, Lucas Heights, 2234, Australia*
[c] *School of Biological, Earth and Environmental Sciences, UNSW Sydney, NSW, Australia*

ARTICLE INFO

Keywords:
laminae count
stalagmite
tree rings
geochronology
dynamic time warping

ABSTRACT

The manual identification and count of laminae in layered textures is a common practice in the study of geological records, which can be time consuming and carry large uncertainty for dense or disturbed lamina textures. We present here a novel image analysis approach to detect and count laminae in geoscientific imagery, called WlCount. Based on Dynamic Time Warping and Wavelet analysis, WlCount firstly aligns persistent vertical elements to increase the continuity of the lamina structure. Then, using a graphical interface, the user extracts the most significant signal frequencies and allows the automatic count of the laminae. The software, tested on a series of stalagmite cut images showing different types of laminations and a tree-ring image, provides an estimation of the laminae detection and count comparable to the manual one. WlCount presents as a useful open-source tool to help geoscientists, sensibly speeding up the lamination count process.

CRediT authorship contribution statement

Fabio Oriani: Development of the main ideas, implementation, experiment conception, data analysis and interpretation, manuscript writing and revision. **Pauline C. Treble:** Development of the main ideas, experiment conception, data acquisition, analysis and interpretation, manuscript revision. **Andy Baker:** Development of the main ideas, experiment conception, data interpretation, manuscript revision. **Gregoire Mariethoz:** Development of the main ideas, experiment conception, data interpretation, manuscript revision.

1. Introduction

Laminae or layers are a dominant type of texture in geoscience from the micro to the macro scale. Several types of geoscientific studies require the quantitative analysis of laminated structures: for example stalagmite (Baker et al., 2021), tree-ring, coral (Isdale et al., 1998), mollusk (Arkhipkin et al., 2018), lake sediment (Brauer et al., 1999; Gan and Scholz, 2013) and ice core (Sigl et al., 2016) paleoclimate reconstructions have all employed annual laminae counting methods to create or support chronologies (Butler et al., 2013; Hopley et al., 2018). In many cases, lamina structures can be blurry, irregular, or discontinuous. When this is the case, manual identification and counting are usually the most accurate means of characterizing these structures, but it is also very time consuming and can involve multiple operators.

This task can be supported by automatic counting techniques based on signal processing (Lotter and

ORCID(s): 0000-0002-8619-4680 (F. Oriani)

Lemcke, 1999; Taylor et al.). These approaches consider an image containing laminations. The expert draw a transect perpendicular to the laminae to extract a time series of the intensity signal. The time series is then processed to identify peaks corresponding to each lamina. This can be based on band-pass filters and minima/maxima detection (Weber et al., 2010; Nagra et al., 2017), fuzzy logic (Ebert and Trauth, 2015), and wavelet transform to extract the component of the signal with a prescribed frequency (e.g. annual periodicity) (Smith et al.). These techniques require repeating the analysis using multiple transects to account for the laminae variability and sometime involve a preliminary assumption on the growth rate. A more sophisticated approach, tested with success on varve sediments (Fabijańska et al., 2020), uses a deep neural network to identify laminae in the target images. This has the advantage of being capable to analyse entire 2D images, but it requires a large training dataset of similar lamination patterns and an accurate setup phase. While these kinds of approaches are promising to assist the counting of laminated structures, there is considerable scope for improvement in developing user-friendly efficient methods. For example: simplification of the preliminary operations to extract the time series, reduction in the need for user-led assumptions in the setup, and techniques to accommodate variable laminae size and density.

An alternative approach to analyze different structured signals, as laminated patterns, is Dynamic Time Warping (DTW). Originally introduced in the late 1970's (Sakoe and Chiba, 1978), DTW is a technique used to compare different time series or more generally data vectors, and apply continuous deformations to align them to match common features such as similar sequences of peaks. Based on the amount of deformation applied to match the data series, the level of similarity of the signals is quantified. This approach has been recently used for a variety of applications in geoscience: to estimate travel time in hydrological time series (Claure et al., 2018), to identify common features in physical logs (Silversides and Melkumyan, 2016), for seismic pattern classification (Orozco-Alzate et al., 2015), in correlations of stratigraphic sections (Ajayi et al., 2020), and to compare paleoclimate proxy time series (Ajayi et al., 2020; Burstyn et al., 2021).

Using the potential of the DTW technique, we present here a novel semi-automatic tool called WlCount. The goal is to assist scientists through the detection and counting process with a simple workflow supported by a graphical user interface (GUI). In contrast to existing techniques, WlCount extract information from a whole given image instead of a given transect. To do that, we introduce an initial automatic stage where, using DTW, the raster image is deformed to reach the vertical alignment of the laminae. The pixel rows in the image are then summed along the column axis to obtain a time series of the signal along the laminae growth direction, from which a chronology may be derived. This avoids the need for a user to choose a particular transect for counting, which may be ambiguous, and reduces uncertainty by retaining only the persistent laminated structure from the local noise. In a second stage, the time series is decomposed with

the wavelet transform and, with the help of the GUI, the user can isolate the signal component which corresponds to the laminae structure. The extracted signal is then automatically thresholded to identify the laminae, whose location is marked in real time in the image. This way, the user can repeat the process to improve the laminae detection.

The proposed approach is primarily tested on a series of pictures obtained by synchrotron radiation x-ray fluorescence mapping (SR-XFM) over annually laminated stalagmites (Golgotha Cave, Yonderup Cave, and Harrie Wood Cave, Australia). The obtained automatic count is compared both visually and statistically with a manual count. The main goal is to assess the ability of the method to reproduce the manual count over a selection of maps in which the laminae vary in size, clarity and amplitude. To test the potential for other applications in the geoscience domain, an additional laminae-detection test is performed on an tree-ring image from a dendrochronological tree stem sample.

The paper is structured as follows: section 2 presents the method and the implementation, in section 3 and 4 the images used and the test methods are described, the results are presented in section 5 and discussed in section 6, and concluding remarks are given in section 7.

2. Methods

WlCount is a novel approach based on image analysis and signal processing with the goal of assisting geoscientists in the identification and counting of laminae represented in raster images. The depicted laminae may have a variable orientation, but preferably sub-vertical (see point 3). The workflow, implemented in python, is composed of the following steps:

Input : raster image of size n rows $\times$ m columns, which can be multivariate (Figure 1 a).

1. If the image is multivariate (e.g. RGB or multiband), the mean value across all variables for each pixel is computed to obtain a univariate image (Figure 1 b).
2. A fixed 5-pixel moving-average filter can be applied as optional preprocessing step to remove small-scale noise and improve the visibility of relevant structures (Figure 1 c).
3. Using the dynamic time-warping technique (DTW, section 2), each pixel row is deformed to obtain a vertical alignment of the laminae (Figure 1 d), preserving the structure coherence from row to row. To assure convergence in the DTW alignment, the deformation is by default limited in a radius of 10 pixels. In preliminary tests (not shown here) this limitation assured a correct alignment in all cases showing a continuous laminae deformation not exceeding +-45 degrees from the column axis.
4. The aligned image is averaged along the column axis (along lamina) to obtain a unique time series (Figure 1 d, red line) of length m, showing the amplitude structures related to the seasonal information,

observed along the row direction. In the time series, each lamina is represented by a wave of a certain length and magnitude.

5. The time series is decomposed using the discrete wavelet transform (Daubechies, 1988; Mallat, 1989): the signal is convoluted with a wavelet, i.e. a theoretical function defined over a limited support and characterized by a certain scale length. The convolution allows obtaining the signal component of the time series in the same scale length as the wavelet. The wavelet is defined for different scale lengths and convoluted each time over the time series. The result is a 2D image where each row represents the intensity of the signal component for a certain scale length (Figure 1 e).
6. The original image, the aligned image with the associated time series, and its wavelet transform are shown in an interactive GUI: at this point the user can draw, with the mouse pointer from left to right, a section over the wavelet image (Figure 1 e, dashed red line) to select the specific signal component corresponding to the annual laminae wavelength. If the section is drawn in the upper part of the wavelet image, dense/small laminae structures are detected, while large-scale laminations are detected if the section is drawn in the lower part (the scale length is indicated in the y axis). The line can be composed of multiple contiguous segments, which allows detection of laminae that are varying in thickness across the image. As explained in the following step, the result of this operation in terms of detected laminae can be immediately checked and repeated if necessary.
7. At every segment drawn, the corresponding portions of wavelet signal are retrieved (Figure 1 f, red curve). Its mean intensity is computed and used as threshold to identify the positive half waves indicating the laminae presence in the image. If the selected wavelet component portion is close to stationary, this simple threshold method is usually sufficient to detect the laminae. The mid-point of each positive half wave is marked as a lamina with a cross in the aligned image (Figure 1 f, red crosses). The user can undo/redo each segment to improve the result.
8. Once the process reaches a point that the user is satisfied with the laminae identification, the section can be ended by a keyboard command, which displays the counts. Multiple lines can be drawn in the wavelet image to assess the uncertainty over different counts.

Output : .dat file containing the coordinates of each count series, python .npy files for the extracted time series and aligned image (points 3 and 4), and a .pdf screenshot of the GUI.

2.1. Laminae alignment by DTW

In the WlCount workflow, every pixel row composing the image intersects the subvertical laminae structures, thus constitutes a data vector containing the laminae fluctuations. DTW (dtaidistance implementation

Table 1
Summary of the metadata of the stalagmite sections used in the tests.

Section ID	Location	x-axis length [mm]	Image size [pixels]	pixel size [μm]
1562	Yonderup Cave, SWWA	19.1	125 × 4775	4.0
1563	Golgotha Cave, SWWA	4.2	1250 × 2100	2.0
23261	Golgotha Cave, SWWA	18.0	300 × 4500	4.0
23262	Golgotha Cave, SWWA	26.0	150 × 3250	8.0
23265	Harrie Wood, NSW Alps	21.0	140 × 2100	10.0

(Meert et al., 2020)) is applied iteratively to deform all pixel rows to obtain a vertical alignment of the laminae structure in the image (section 2 step 3). This is applied to pairs of rows in a hierarchical fashion (Figure 2): DTW is applied to the first row of the image to match the second one, then to the third to match the fourth, and so on. This way, all the pairs of adjacent rows are aligned with each other (if the number of rows are odd the last one is discarded). At this point, the numerical values in the two rows of each pair are averaged to obtain a unique row. Applying the averaging to all pairs results in an image composed by half the number of pixel rows. Next, DTW is applied again, aligning the new row pairs and averaging to obtain half the number of rows. The process is repeated until one single pixel row remains, consisting in the time series of step 4 in the WlCount workflow. For display purposes, every original pixel row is again deformed to match this time series and obtain a visible aligned image (Figure 1 d).

3. Used data

The imagery used to test the WlCount technique consists of a series of SR-XFM generated maps (XFM Australian Synchrotron, Howard et al., 2020) obtained from polished slabs sectioned along the growth axis of cave stalagmites, sampled from underground caves in New South Wales (NSW) and South West Western Australia (SWWA). For all images (Figure 3), the Strontium (Sr) relative element concentration map is used for the automatic counting since in this case it shows the laminated structure most clearly. The 8-bit RGB intensity levels are based on the instrumental levels of light detection, with zones of high element concentration displayed with light shades. The maps length varies from 4 to 26 mm with a pixel resolution of 2-10 micrometers (Table 1). The represented laminated textures are of different types, including thin well-defined laminae (1562), thick irregular (23265), barely visible (1563) or disturbed by porosity (23261 and 23262).

The tree-ring sample used in the last experiment is the test image used in the demonstration of the MtreeRing software (Shi et al., 2019). The images used in this analysis are increment core samples from coniferous species (Larix gmelinii) in the northern Greater Khingan Mountains (Heilongjiang Province, NE China).

4. Validation

The proposed technique is tested by operating the WlCount software on all test images and performing 3 counts for each image. The laminae are counted and their position marked in the aligned section with a series of cross pointers. The position (x coordinate) and number of the detected laminae is then compared to a manual count (MC), used as reference. Being the MC repeated by different operators, an uncertainty value (+- integer) is related to the number of laminae which have not been constantly detected over repeated counts, being weakly prominent or discontinuous. Following (Faraji et al.), two codes for uncertain counts are considered: code 1 if a lamina presents a relative (0-1) detection frequency in the range $[0.51 - 0.95]$ and code 2 for the range $[0.06 - 0.50]$. The corresponding error on the count of each uncertain lamina is determined as $1 - (p1 + p2)/2$, with $[p1, p2]$ as the frequency range. Therefore, for every code-1 and code-2 lamina the error contribution is respectively 0.27 and 0.72. The sum of these unitary contributions constitutes the MC error.

To make a quantitative comparison between the automatic and manual counts, two statistical indicators have been considered: i) the number of laminae counted with WlCount is compared to the MC and its uncertainty range and ii) the average distance (Da) is computed between the manually counted laminae to the closest laminae detected with WlCount. Da allows assessing whether the spatial laminae distribution obtained from WlCount is similar to the one from the MC. If this distance is lower than the mean laminae thickness (Ta), this suggests the spatial distribution of the detected laminae follows the actual laminae distribution. Ta is estimated as $(x_{start} - x_{end})/(\mathrm{MC} - 1)$, where x_{start} and x_{end} are the first and last lamina x coordinates detected by MC.

5. Results

As visual examples of the WlCount software GUI, the output display for the counts on sections 1562 and 23265 are shown in Figure 4 (all output displays attached as supplemental material). The output display shows the original image (mean of all variables if multivariate) at the top, the aligned image in the center together with the time series describing the laminae variations along the x axis, and the wavelet transform of the same time series at the bottom. Section 1562 (Figure 4 a) presents a thin laminae structure in varying density and signal intensity. Avoiding the MA preprocessing (section 2 step 2), allows preserving the fine-scale details for the alignment (Figure 4 a, center image). The alignment process improves the visibility and continuity of thin and barely visible vertical structures, whose signal is contained in the final time series (red line). The wavelet transform of this time series (Figure 4 a, bottom image) shows a marked periodicity in the wavelet scale range of 3-6 pixels (y axis), which corresponds to the laminae structure. By drawing

segmented lines in the wavelet transform image, the user isolates this signal component. It is then used by the software to detect the laminae presence in the upper image and return the amount (235-293 bands).

The second example (Figure 4 b) shows the output display for section 23262. In this case, the laminae structure appears thicker because the section is approximately half the length with respect to section 1562 (the image is stretched to occupy the whole display). The user choose to apply the MA preprocessing which removed the small-scale noise, resulting in a smoother image and time series. In the wavelet transform image (Figure 4 bottom), the choice of the wavelet component with scale length of 2 pixels allowed detecting 99 laminae, marked in the aligned image. The image alignment improved again the continuity of the laminae structures. Note that the three lines in the wavelet transform are superposed but they are formed by different segments. This allows breaking up the wavelet signal in different parts which are thresholded differently using their mean value. The final laminae count is equivalent but small differences appear in the laminae locations (crosses of different colors in Figure 4 b, center image).

Figure 5 shows all the test sections with reference manual laminae count (MC) and the WlCount estimations (three attempts per section). All laminae detected in the MC (blue crosses) are linked to the closest WlCount detection by a dashed white segment. For all sections, the WlCount laminae distribution is overall similar to the MC, but some mismatch in the detection can occur, as visible in Figure 5 b and e: Wlcount may count twice an MC lamina or vice versa. This result is confirmed by the statistical scores in Table 2. Sections 1562 and 1563 present respective MC values of 246 and 131 with a relatively small uncertainty (+- 12 and +-19), while the WlCount estimations are in part within and in part outside this uncertainty range (Table 2 bold values). For sections 23261 and 23262 the laminae are dense, less continuous, and more disturbed by porosity (Figure 5 c and d). For these images, the MC uncertainty is higher (+-43 and +-85) and all WlCount estimations lie within the same range. Section 23265 presents better defined laminae for which the MC and Wlcount match well with very low uncertainty (98+-5 and 99 respectively).

For all counts, the average distance between every MC detection and the closest WlCount detection (Da in Table 2) is sensibly lower than the average laminae thickness (Table 2 Ta). This suggests that the laminae locations detected by WlCount match on average the MC locations.

The last test image shows a ring lamination from a cross section of tree-ring sample. With respect to the previous stalagmite images, the laminated pattern here is more regular and the border clearer, which makes the detection and counting task easier. As confirmed by the visual output (Figure 6), WlCount is able to detect efficiently all the rings and provide the exact count. Note that here, the laminae thickness is larger and the associated wavelet frequency is represented in the central part of the wavelet transform image, which has been captured with a unique threshold line. The presence of discontinuities in the ring

Table 2
Summary of the results on the counts on all sections, including: the section ID, the different counts (#) performed using WlCount, the reference manual count (MC) with uncertainty range, the average laminae thickness (Ta), the average distance between MC laminae and the closest WlCount laminae (Da), and the use of the moving-average (MA) preprocessing (step 2 section 2). MC is a unique value with uncertainty for every section. WlCount counts outside the MC uncertainty range are indicated in bold.

Section ID	WlCount #	MC [laminae]	WlCount [laminae]	Ta [pixels]	Da [pixels]	use of MA
1562	0	246+-12	235	19.48	5.78	no
	1		**293**		4.44	no
	2		235		5.28	no
1563	0	131+-19	127	15.72	5.03	yes
	1		**154**		4.10	yes
	2		**96**		6.46	yes
23261	0	245+-43	269	12.81	4.68	no
	1		208		5.87	no
	2		247		5.12	no
23262	0	351+-85	324	8.21	2.78	no
	1		327		2.62	no
	2		322		2.81	no
23265	0	98+-5	99	20.03	5.78	yes
	1		99		6.11	yes
	2		99		5.75	yes

border (thin stripes in blue shaded zones) does not affect the ring detection.

6. Discussion

In contrast to previous techniques for geoscientific laminae counting (section 1), which are mainly based on time series analysis from linear transects, the workflow introduced here is, to our knowledge, the first laminae-counting tool which extracts information from a whole given image with no training phase. The pairwise hierarchical application of the DTW alignment (section 2 step 3) allows estimating the laminated structure based on the average thickness and location of signals persistent along the column direction. Both counts displayed in Figure 4 show how the hierarchical DTW not only aligns the subvertical or curved structures, but allows increasing their continuity over local disturbances, which shrink and tend to disappear in the aligned images. The results show that this approach is adaptive to textures of different thickness, including discontinuous, disturbed, or barely visible laminae, which can constitute a primary limitation for pattern-recognition techniques (see e.g. Fabijańska et al., 2020).

Instead of a non-supervised technique requiring a setup process, WlCount is designed to be supervised with an graphical interface, relying on the scientist knowledge on the studied morphology. This requires the user to become familiar with the wavelet analysis and the choice of the appropriate component from the wavelet image. On the other hand, the process is quite intuitive since the laminae periodicity match their spatial distribution and it is selected manually with a trace. The resulting laminae detection appears on the

display, allowing quick corrections.

The optional MA preprocessing, e.g. used for section 23265 (Figure 4 b), can improve the visibility of the structures by removing small-scale noise, which can generate vertical artifacts in the alignment image. However, this noise is usually filtered out in the wavelet analysis by choosing the appropriate wavelet component. The MA preprocessing is not suggested if thin (< 5 pixels) laminae are present, e.g. section 1562 (Figure 4 a).

The results suggest that the WlCount estimation is comparable to the manual count for both the number of detected laminae and their position (Table 2). The uncertainty of the WlCount estimation can be given by tracing multiple trajectories in the wavelet space, to explore the zone representing the laminae fluctuation. In case of high uncertainty, the WlCount estimation can constitute a baseline assessment which can be further examined and manually edited using the output files.

Tested on high-resolution images of 10^6 pixels (Table 1), the technique took up to 5 minutes to generate one aligned image on a personal computer. This phase can be skipped when the software is run again on the same image, by using the previous alignment files which are automatically stored and recalled from the local folder. The alignment algorithm (Section 2 step 3) is mainly non-sequential, so it can be parallelized for cluster computing if needed. Examining the images and choosing the wavelet component takes usually some minutes, while manual count can take up to hours for one single count.

We now compare WlCount to other lamina counting approaches and consider its applicability in geoscience. Previously proposed approaches based on Markov chains (Winstrup et al., 2012) allow a more rigorous quantification of the uncertainty in the layer identifications. Nevertheless, they require statistical assumptions on the layer thickness and a set of layer templates to calibrate the algorithm. This probabilistic approach, tested on chemical time series from ice cores, is convenient for long and stationary scan-line data exhibiting relatively regular lamination structures, for which an accurate inspection is impractical. Conversely, WlCount requires to visualize entirely the data under form of 2D images, but it is adaptive to more diverse and non-stationary lamination structures, with no required calibration phase and a relatively fast operation.

The test on the tree-ring image (Figure 6) shows that the proposed technique can easily detect tree-ring laminations. With respect to the MtreeRing algorithm, tested on the same image (Shi et al., 2019) with comparable results to the commercial software WinDENDRO™, WlCount does not require tracing a scan line perpendicular to the ring borders. This is not necessary since the average laminae location and thickness is represented in the aligned image (Figure 1 d). Moreover, the WlCount approach is less affected by discontinuity in the ring patterns, since the time series extracted from the image is not based

on segmentation as in MtreeRing. The WlCount implementation can be adapted to dendrochronological applications by generating as output data not only a time series of band center coordinates, but also the border coordinates and ring thickness.

The proposed approach can also have a potential in the field of sclerochronology (Hudson et al., 1976), which analyzes laminar growth patterns in skeletal tissue samples of mollusks and fishes (Schöne, 2013). These laminae, often curved and poorly defined, can benefit from the hierarchical DTW technique, which enhances the visibility of the persistent features in the vertical laminae alignment. This can also reduce potential bias due to the discard of samples presenting discontinuous or unclear lamination, which can be relevant since possibly correlated to environmental conditions (Peharda et al., 2021).

7. Conclusions

The analysis of laminated structures in geoscientific imagery is a common task to acquire information on geochronology and periodic natural processes. In this paper, we introduced WlCount as a novel semi-automatic laminae counting method, with the goal of speeding up and supporting laminae detection counting operations. With respect to the available assisted or automatic count approaches, the novelty of WlCount resides in the extraction of the average features of the laminated structure from a whole given image, without the need of tracing and comparing multiple line scans and minimizing the effect of disturbances and discontinuities.

By applying Dynamic Time Warping to pairs of pixel rows in the image, the technique aligns vertical structures and extracts a time series of the longitudinal variations. This time series is then decomposed using the wavelet transform, which generates a 2D image describing the longitudinal variations at different scales. From the GUI, the user selects the wavelet component representing the longitudinal variations corresponding to the laminated structures. This component is then automatically thresholded to detect the laminae position in the section image.

Tested on a series of different images from cave stalagmites, WlCount returned a laminae number and position similar to the reference manual count for both the laminae number and their location. The uncertainty of the count can be assessed by performing different wavelet component selections in the scale range representative of the laminae fluctuations. This allows comparing the number and positions of the detected laminae for different counts. The output detection data can be further examined and manually edited if needed. The last test on a tree-ring image suggests the potential of WlCount in other geoscientific fields as the one of dendrochronology, but further testing is needed and possibly an adaptation of the produced output data.

Overall, WlCount presents as a flexible tool to make a quick assessment on the number and spatial distribution of the laminae on the studied images, with an accuracy and reliability comparable to the manual count, but a minimal user intervention. Future development will include further testing and adaptation of the implementation to specific applications.

316 **Code availability section**

317 Name of the code/library: WlCount

318 Contact: Fabio Oriani, University of Lausanne, fabio.oriani@protonmail.com

319 Suggested Hardware requirements: processor frequency 3.60+ GHz, 8+ GB memory

320 Program language: Python 3

321 Software required: Phyton 3 with additional open-source packages (see repository)

322 Program size: 1.2 GB (whole repository)

323 The source codes are available for downloading at the link:

324 https://bitbucket.org/orianif/wlcount/src/master/

325 **Acknowledgments**

326 The micro-XRF analysis research was undertaken on the X-ray fluorescence microscopy (XFM) beamline
327 at the Australian Synchrotron, part of ANSTO under proposals PA13457 and PA14312.

328 References

329 Ajayi, S., Kump, L.R., Ridgwell, A., Kirtland Turner, S., Hay, C.C., Bralower, T.J., 2020. Evalua-
330 tion of Paleocene-Eocene thermal maximum carbon isotope record completeness? An illustration of the po-
331 tential of dynamic time warping in aligning paleo-proxy records. Geochemistry, Geophysics, Geosystems
332 21, e2019GC008620. URL: https://agupubs.onlinelibrary.wiley.com/doi/abs/10.1029/2019GC008620, doi:10.1029/
333 2019GC008620, arXiv:https://agupubs.onlinelibrary.wiley.com/doi/pdf/10.1029/2019GC008620.

334 Arkhipkin, A.I., Bizikov, V.A., Doubleday, Z.A., Laptikhovsky, V.V., Lishchenko, F.V., Perales-Raya, C., Hollyman, P.R.,
335 2018. Techniques for estimating the age and growth of molluscs: Cephalopoda. Journal of Shellfish Research 37, 783 – 792.
336 URL: https://doi.org/10.2983/035.037.0409, doi:10.2983/035.037.0409.

337 Baker, A., Mariethoz, G., Comas-Bru, L., Hartmann, A., Frisia, S., Borsato, A., Treble, P.C., Asrat, A.,
338 2021. The properties of annually laminated stalagmites - a global synthesis. Reviews of Geophysics
339 59, e2020RG000722. URL: https://agupubs.onlinelibrary.wiley.com/doi/abs/10.1029/2020RG000722, doi:10.1029/
340 2020RG000722, arXiv:https://agupubs.onlinelibrary.wiley.com/doi/pdf/10.1029/2020RG000722.

341 Brauer, A., Endres, C., G, C., Litt, T., Stebich, M., Negendank, J.F., 1999. High resolution sediment and vegetation responses
342 to Younger Dryas climate change in varved lake sediments from Meerfelder Maar, Germany. Quaternary Science Reviews 18,
343 321–329. URL: https://www.sciencedirect.com/science/article/pii/S0277379198000845, doi:10.1016/S0277379198000845
344 00084-5.

345 Burstyn, Y., Gazit, A., Dvir, O., 2021. Hierarchical dynamic time warping methodology for aggregating multiple geolog-
346 ical time series. Computers & Geosciences 150, 104704. URL: https://www.sciencedirect.com/science/article/pii/
347 S0098300421000194, doi:10.1016/j.cageo.2021.104704.

348 Butler, P.G., Wanamaker, A.D., Scourse, J.D., Richardson, C.A., Reynolds, D.J., 2013. Variability of marine climate on the
349 North Icelandic Shelf in a 1357-year proxy archive based on growth increments in the bivalve Arctica islandica. Palaeo-
350 geography, Palaeoclimatology, Palaeoecology 373, 141–151. URL: https://www.sciencedirect.com/science/article/pii/

S0031018212000302, doi:10.1016/j.palaeo.2012.01.016. Unraveling environmental histories from skeletal diaries - advances in sclerochronology.

Claure, Y.N., Matsubara, E.T., Padovani, C., Prati, R.C., 2018. Polywatt: A polynomial water travel time estimator based on derivative dynamic time warping and perceptually important points. Computers & Geosciences 112, 54–63. URL: https://www.sciencedirect.com/science/article/pii/S009830041731261X, doi:10.1016/j.cageo.2017.12.002.

Daubechies, I., 1988. Orthonormal bases of compactly supported wavelets. Communications on pure and applied mathematics 41, 909–996. doi:10.1002/cpa.3160410705.

Ebert, T., Trauth, M.H., 2015. Semi-automated detection of annual laminae (varves) in lake sediments using a fuzzy logic algorithm. Palaeogeography, Palaeoclimatology, Palaeoecology 435, 272–282. URL: https://www.sciencedirect.com/science/article/pii/S0031018215002886, doi:10.1016/j.palaeo.2015.05.024.

Fabijańska, A., Feder, A., Ridge, J., 2020. DeepVarveNet: Automatic detection of glacial varves with deep neural networks. Computers & Geosciences 144, 104584. URL: https://www.sciencedirect.com/science/article/pii/S0098300420305707, doi:10.1016/j.cageo.2020.104584.

Faraji, M., Borsato, A., Frisia, S., . Accurate dating of stalagmites from low seasonal contrast tropical Pacific climate using Sr 2D maps, fabrics and annual hydrological cycles. Sci Rep 11, 2178. doi:10.1038/s41598-021-81941-x".

Gan, S.Q., Scholz, C.A., 2013. Extracting paleoclimate signals from sediment laminae: An automated 2-D image processing method. Computers & Geosciences 52, 345–355. URL: https://www.sciencedirect.com/science/article/pii/S0098300412003652, doi:10.1016/j.cageo.2012.10.016.

Hopley, P.J., Weedon, G.P., Brierley, C.M., Thrasivoulou, C., Herries, A.I., Dinckal, A., Richards, D.A., Nita, D.C., Parrish, R.R., Roberts, N.M.W., Sahy, D., Smith, C.L., 2018. Orbital precession modulates interannual rainfall variability, as recorded in an Early Pleistocene speleothem. Geology 46, 731–734. URL: https://doi.org/10.1130/G45019.1, doi:10.1130/G45019.1, arXiv:https://pubs.geoscienceworld.org/gsa/geology/article-pdf/46/8/731/4831717/731.pdf.

Howard, D.L., de Jonge, M.D., Afshar, N., Ryan, C.G., Kirkham, R., Reinhardt, J., Kewish, C.M., McKinlay, J., Walsh, A., Divitcos, J., Basten, N., Adamson, L., Fiala, T., Sammut, L., Paterson, D.J., 2020. The XFM beamline at the Australian Synchrotron. Journal of Synchrotron Radiation 27, 1447–1458. URL: https://doi.org/10.1107/S1600577520010152, doi:10.1107/S1600577520010152.

Hudson, J.H., Shinn, E.A., Halley, R.B., Lidz, B., 1976. Sclerochronology: A tool for interpreting past environments. Geology 4, 361–364. URL: https://doi.org/10.1130/0091-7613(1976)4<361:SATFIP>2.0.CO;2, doi:10.1130/0091-7613(1976)4<361:SATFIP>2.0.CO;2, arXiv:https://pubs.geoscienceworld.org/gsa/geology/article-pdf/4/6/361/3541223/i0091-7613-4-6-361.pdf.

Isdale, P.J., Stewart, B.J., Tickle, K.S., Lough, J.M., 1998. Palaeohydrological variation in a tropical river catchment: a reconstruction using fluorescent bands in corals of the Great Barrier Reef, Australia. The Holocene 8, 1–8. URL: https://doi.org/10.1191/095968398670905088, doi:10.1191/095968398670905088, arXiv:https://doi.org/10.1191/095968398670905088.

Lotter, A.F., Lemcke, G., 1999. Methods for preparing and counting biochemical varves. Boreas 28, 243–252. URL: https://onlinelibrary.wiley.com/doi/abs/10.1111/j.1502-3885.1999.tb00218.x, doi:10.1111/j.1502-3885.1999.tb00218.x, arXiv:https://onlinelibrary.wiley.com/doi/pdf/10.1111/j.1502-3885.1999.tb00218.x.

Mallat, S.G., 1989. Multiresolution approximations and wavelet orthonormal bases of l2(r). Transactions of the American Mathematical Society 315, 69–87. doi:10.2307/2001373.

Meert, W., Hendrickx, K., Craenendonck, T.V., 2020. Wannesm/dtaidistance v2.0.0. URL: https://doi.org/10.5281/zenodo.3981067, doi:10.5281/zenodo.3981067.

Nagra, G., Treble, P.C., Andersen, M.S., Bajo, P., Hellstrom, J., Baker, A., 2017. Dating stalagmites in mediterranean climates using annual trace element cycles. Scientific Reports 7, 621. URL: https://doi.org/10.1038/s41598-017-00474-4.

Orozco-Alzate, M., Castro-Cabrera, P.A., Bicego, M., Londo1o-Bonilla, J.M., 2015. The dtw-based representation space for seismic pattern classification. Computers & Geosciences 85, 86–95. URL: https://www.sciencedirect.com/science/article/pii/S0098300415001387, doi:10.1016/j.cageo.2015.06.007.

Peharda, M., Sch6ne, B.R., Black, B.A., Corr8ge, T., 2021. Advances of sclerochronology research in the last decade. Palaeogeography, Palaeoclimatology, Palaeoecology 570, 110371. URL: https://www.sciencedirect.com/science/article/pii/S0031018221001565, doi:10.1016/j.palaeo.2021.110371.

Sakoe, H., Chiba, S., 1978. Dynamic programming algorithm optimization for spoken word recognition. IEEE Transactions on Acoustics, Speech, and Signal Processing 26, 43–49. doi:10.1109/TASSP.1978.1163055.

Schöne, B.R., 2013. Arctica Islandica (Bivalvia): A unique paleoenvironmental archive of the northern North Atlantic Ocean. Global and Planetary Change 111, 199–225. URL: https://www.sciencedirect.com/science/article/pii/S0921818113002130, doi:10.1016/j.gloplacha.2013.09.013.

Shi, J., Xiang, W., Liu, Q., Shah, S., 2019. MtreeRing: An R package with graphical user interface for automatic measurement of tree ring widths using image processing techniques. Dendrochronologia 58, 125644. URL: https://www.sciencedirect.com/science/article/pii/S1125786519301006, doi:10.1016/j.dendro.2019.125644.

Sigl, M., Fudge, T.J., Winstrup, M., Cole-Dai, J., Ferris, D., McConnell, J.R., Taylor, K.C., Welten, K.C., Woodruff, T.E., Adolphi, F., Bisiaux, M., Brook, E.J., Buizert, C., Caffee, M.W., Dunbar, N.W., Edwards, R., Geng, L., Iverson, N., Koffman, B., Layman, L., Maselli, O.J., McGwire, K., Muscheler, R., Nishiizumi, K., Pasteris, D.R., Rhodes, R.H., Sowers, T.A., 2016. The WAIS Divide deep ice core WD2014 chronology – Part 2: Annual-layer counting (0–31 ka BP). Climate of the Past 12, 769–786. URL: https://cp.copernicus.org/articles/12/769/2016/, doi:10.5194/cp-12-769-2016.

Silversides, K.L., Melkumyan, A., 2016. A dynamic time warping based covariance function for gaussian processes signature identification. Computers & Geosciences 96, 69–76. URL: https://www.sciencedirect.com/science/article/pii/S009830041630214X, doi:10.1016/j.cageo.2016.08.001.

Smith, C., Fairchild, I., Spötl, C., Frisia, S., Borsato, A., Moreton, S., Wynn, P., . Chronology building using objective identification of annual signals in trace element profiles of stalagmites. Quaternary Geochronology 4, 11–21. doi:10.1016/j.quageo.2008.06.005.

Taylor, K.C., Alley, R.B., Meese, D.A., Spencer, M.K., Brook, E.J., Dunbar, N.W., Finkel, R.C., Gow, A.J., Kurbatov, A.V., Lamorey, G.W., Mayewski, P.A., Meyerson, E.A., Nishiizumi, K., Zielinski, G.A., . Dating the Siple Dome (Antarctica) ice core by manual and computer interpretation of annual layering. Journal of Glaciology 50, 453–461. doi:10.3189/172756504781829864.

Weber, M.E., Reichelt, L., Kuhn, G., Pfeiffer, M., Korff, B., Thurow, J., Ricken, W., 2010. Bmpix and peak tools: New methods for automated laminae recognition and counting - application to glacial varves from antarctic marine sediment. Geochemistry, Geophysics, Geosystems 11. URL: https://agupubs.onlinelibrary.wiley.com/doi/abs/10.1029/2009GC002611, doi:10.1029/2009GC002611, arXiv:https://agupubs.onlinelibrary.wiley.com/doi/pdf/10.1029/2009GC002611.

Winstrup, M., Svensson, A.M., Rasmussen, S.O., Winther, O., Steig, E.J., Axelrod, A.E., 2012. An automated approach for

427 annual layer counting in ice cores. Climate of the Past 8, 1881–1895. URL: https://cp.copernicus.org/articles/8/1881/
428 2012/, doi:10.5194/cp-8-1881-2012.

List of Figures

1 Sketch of the WlCount workflow. 16
2 Sketch of the hierarchical DTW workflow. In this example, only two levels of alignment are necessary to generate the final time series. 17
3 Synchrotron images of the stalagmite sections used in the tests. The light intensity indicates a higher Sr concentration. 18
4 Example of the WlCount graphic interface section 1562 (a) and 23265 (b). 19
5 Comparison of the detected laminae locations between the reference manual count and WlCount. The white dashed lines indicate connections between manually detected laminae and the closest automatic detections. 20
6 Example of the WlCount application (output display) on a tree-ring image used for dendrochronology. 21

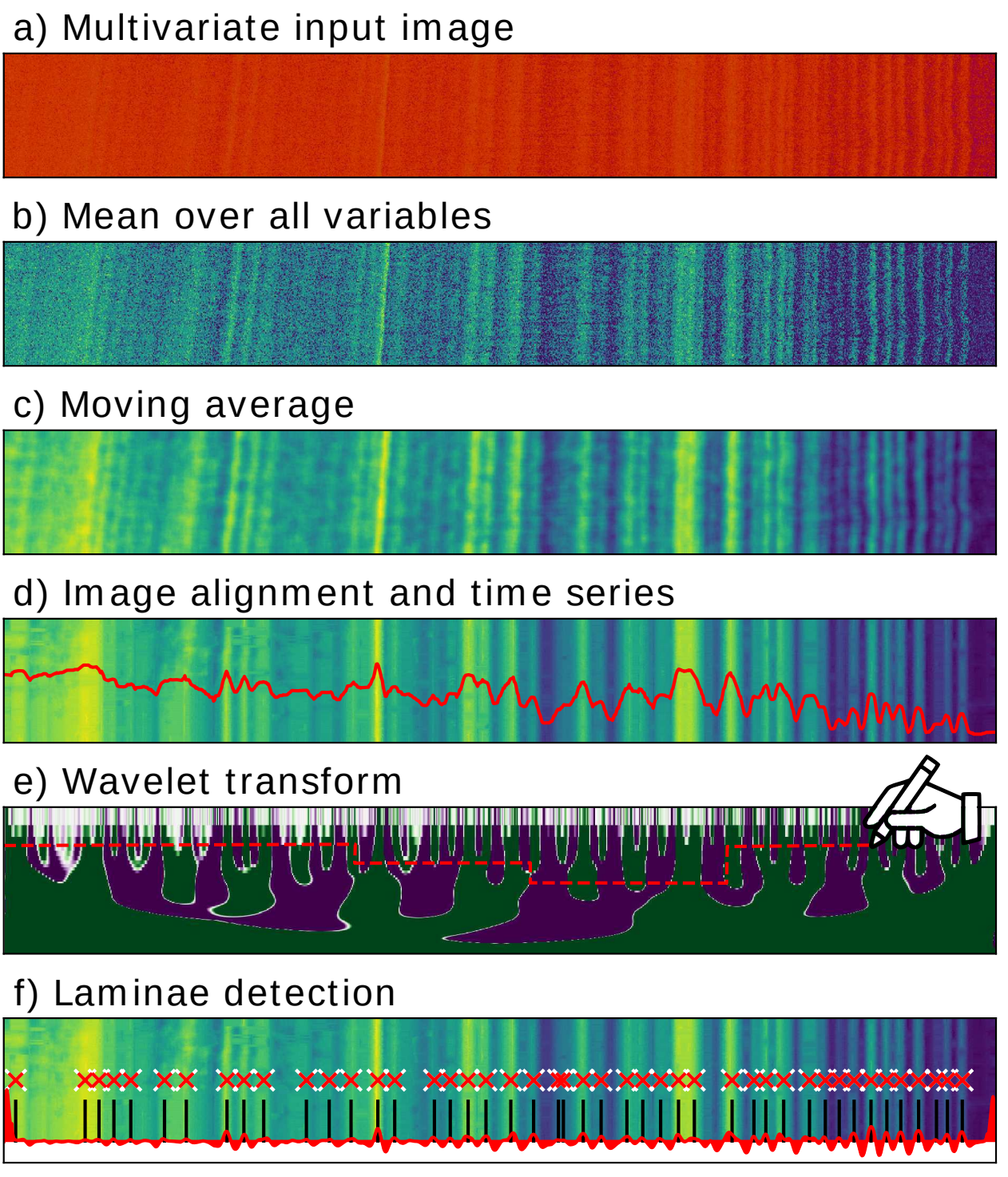

Figure 1: Sketch of the WICount workflow.

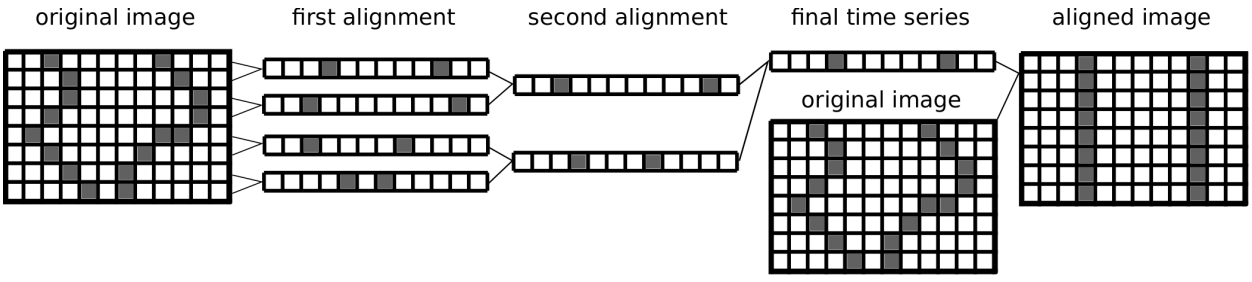

Figure 2: Sketch of the hierarchical DTW workflow. In this example, only two levels of alignment are necessary to generate the final time series.

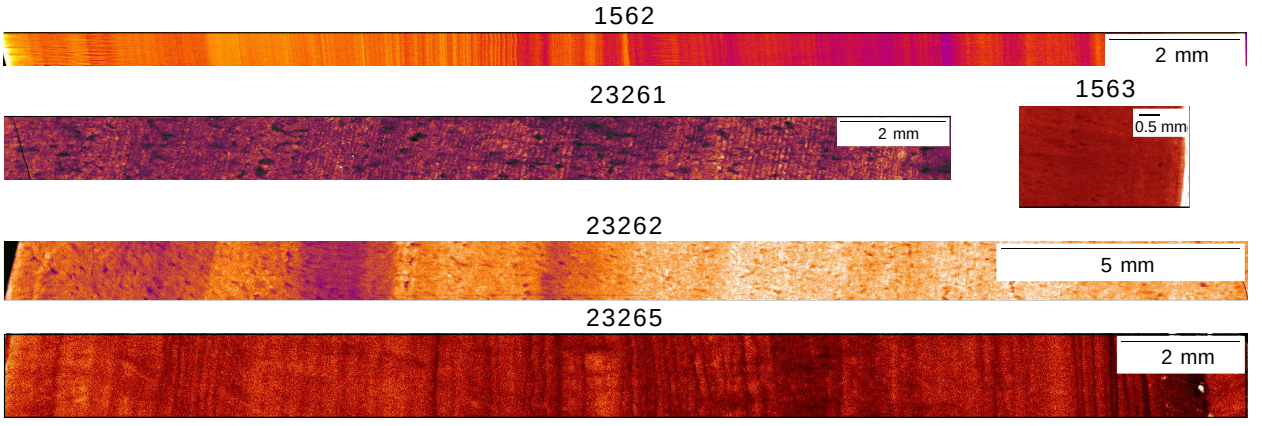

Figure 3: Synchrotron images of the stalagmite sections used in the tests. The light intensity indicates a higher Sr concentration.

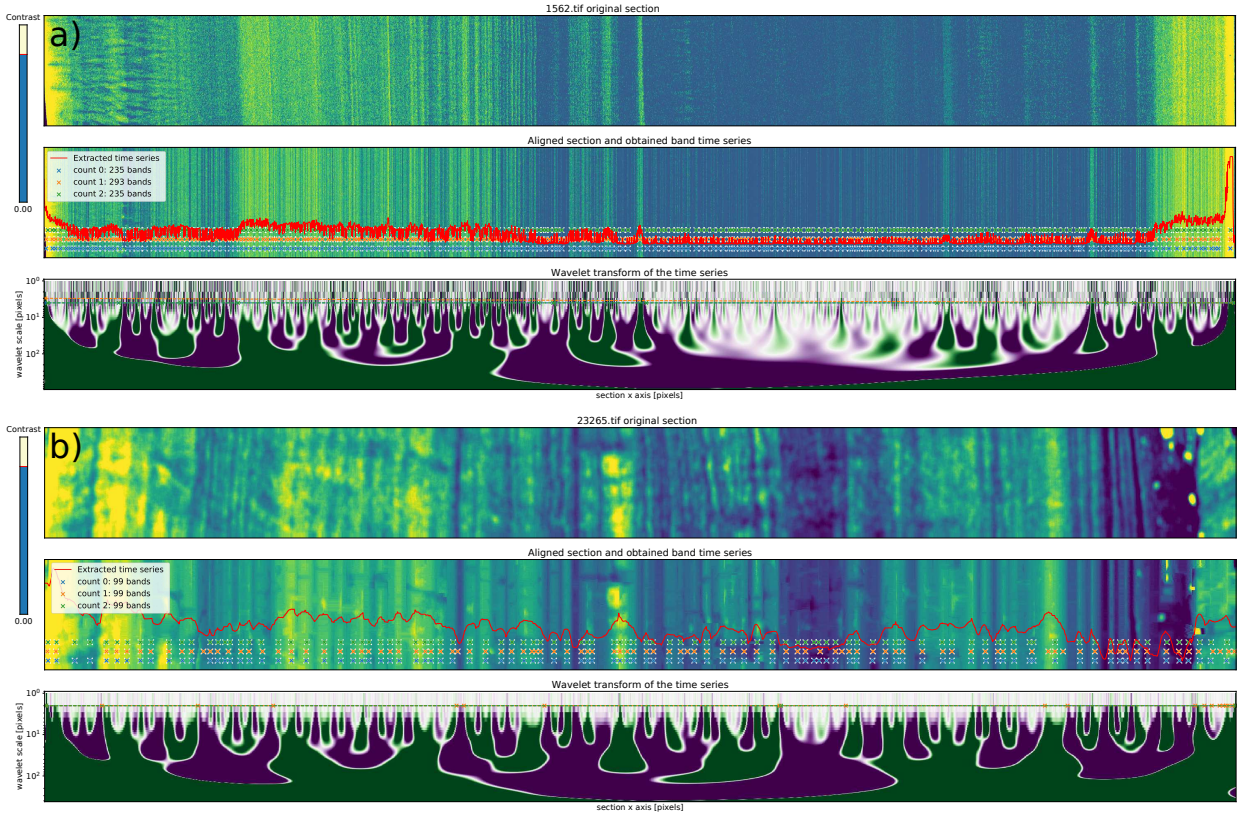

Figure 4: Example of the WICount graphic interface section 1562 (a) and 23265 (b).

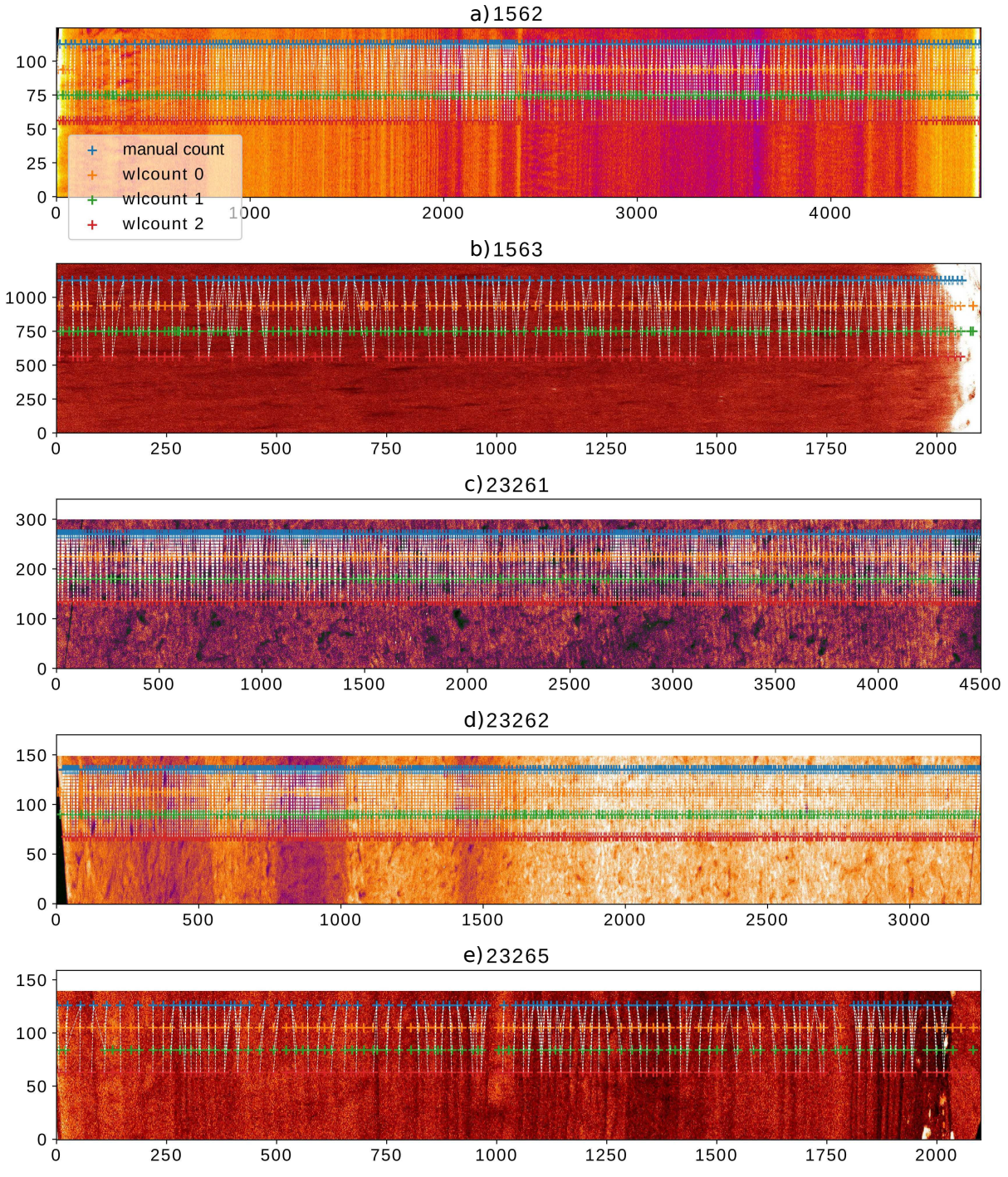

Figure 5: Comparison of the detected laminae locations between the reference manual count and WICount. The white dashed lines indicate connections between manually detected laminae and the closest automatic detections.

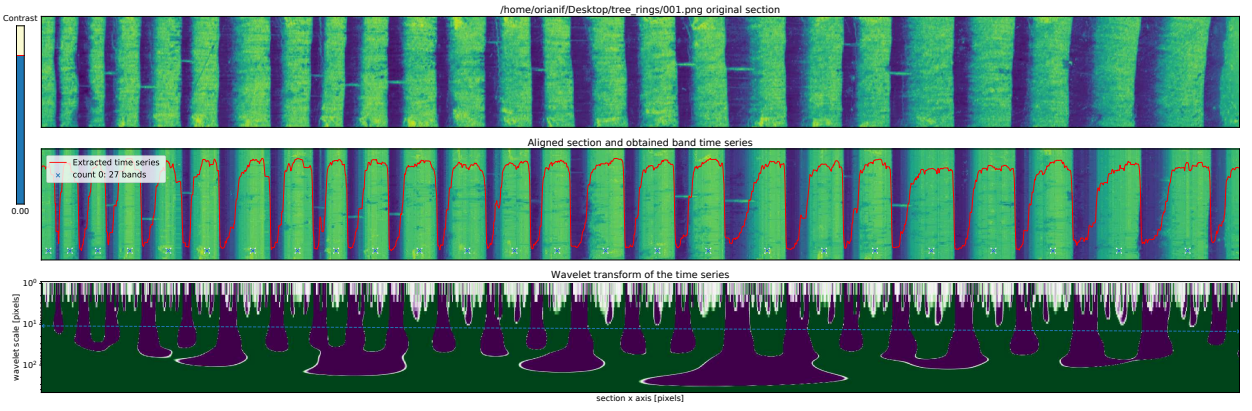

Figure 6: Example of the WICount application (output display) on a tree-ring image used for dendrochronology.

Supplemental material for the manuscript
“WlCount: Geological lamination detection and counting using an image analysis approach”
Fabio Oriani, Pauline C. Treble, Andy Baker, Gregoire Mariethoz

CONTENT:
Output screenshots of the WlCount operation for all stalagmite section images.

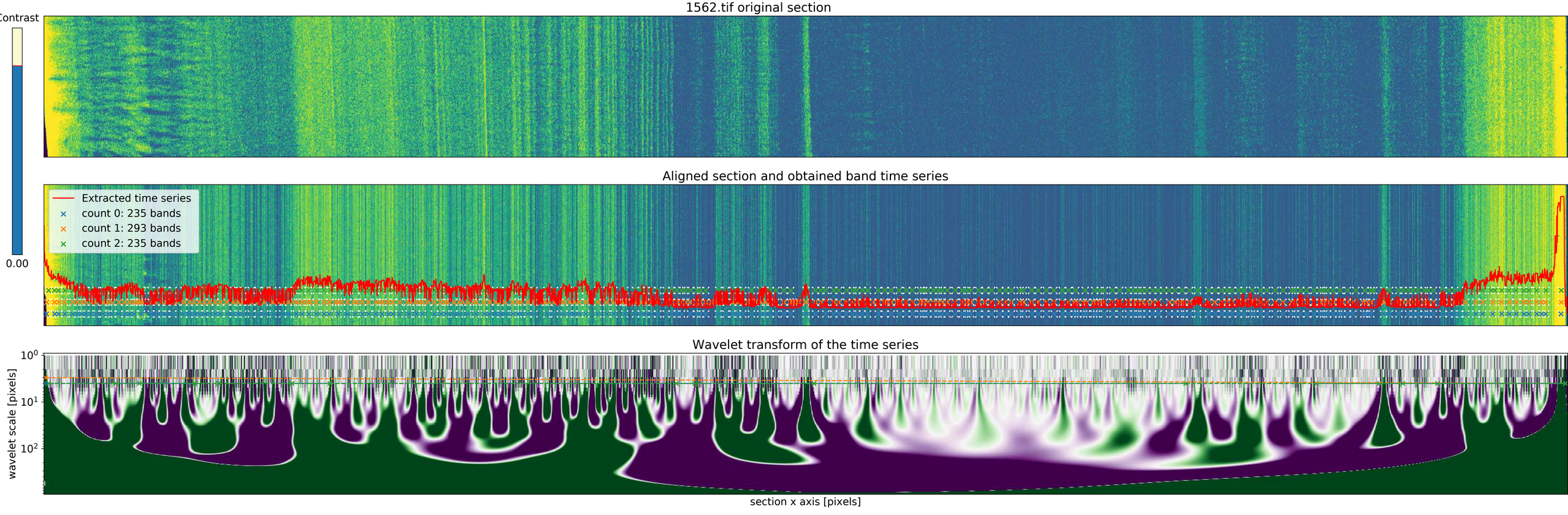
1562.tif original section
Contrast
0.00
Aligned section and obtained band time series
Extracted time series
count 0: 235 bands
count 1: 293 bands
count 2: 235 bands
Wavelet transform of the time series
wavelet scale [pixels]
10^0
10^1
10^2
section x axis [pixels]

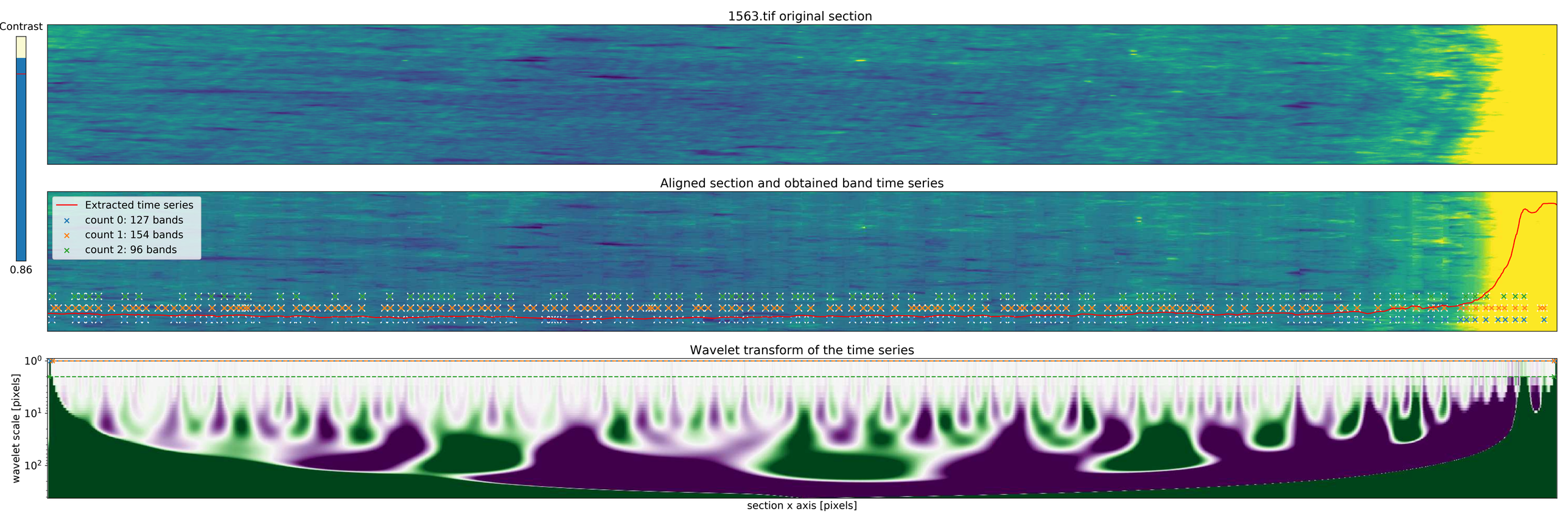
1563.tif original section
Contrast
0.86
Aligned section and obtained band time series
Extracted time series
count 0: 127 bands
count 1: 154 bands
count 2: 96 bands
Wavelet transform of the time series
10^0
10^1
10^2
wavelet scale [pixels]
section x axis [pixels]

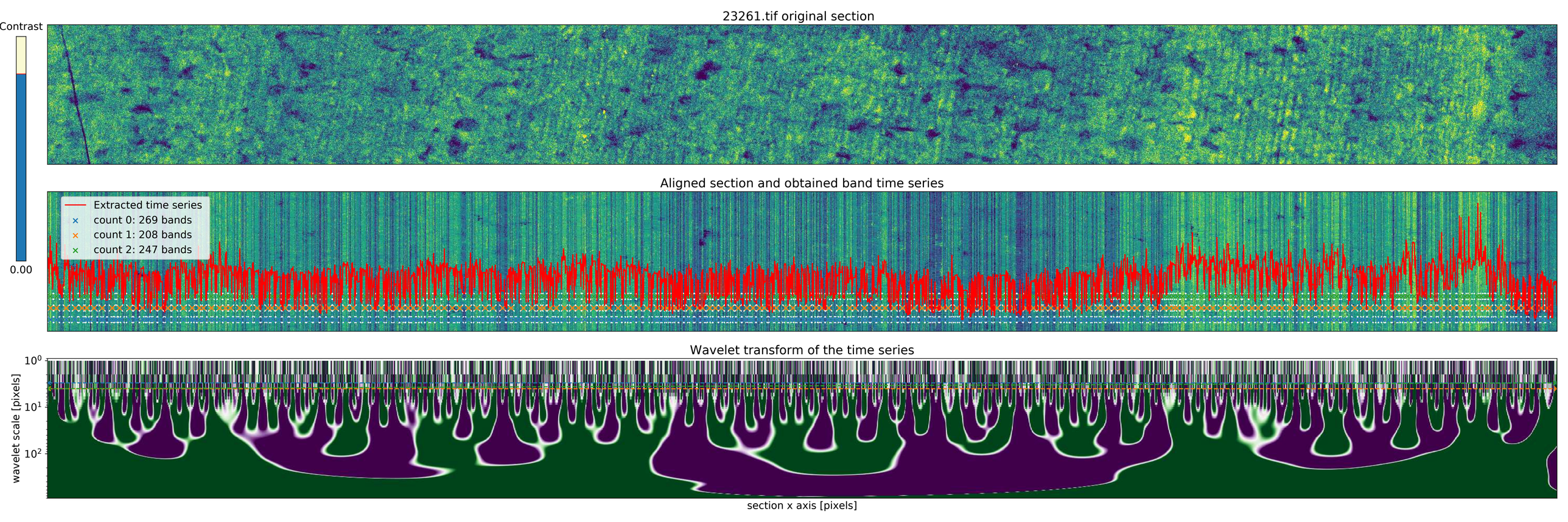
23261.tif original section
Contrast
0.00
Aligned section and obtained band time series
Extracted time series
count 0: 269 bands
count 1: 208 bands
count 2: 247 bands
Wavelet transform of the time series
wavelet scale [pixels]
10^0
10^1
10^2
section x axis [pixels]

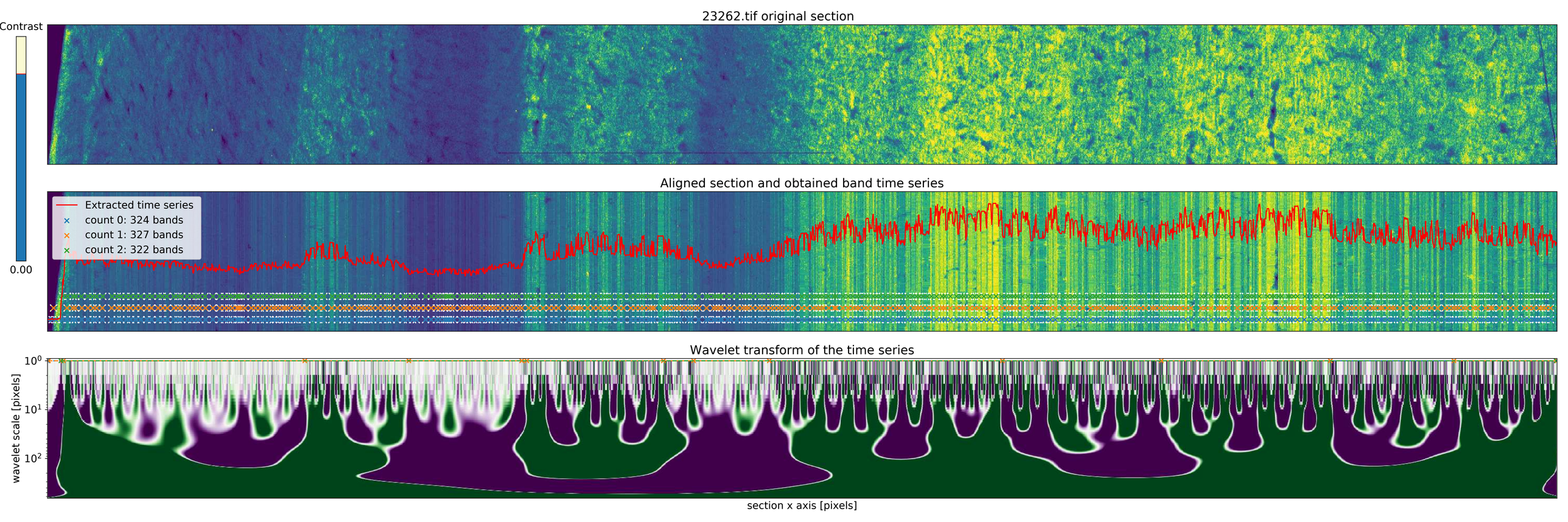
23262.tif original section
Contrast
0.00
Aligned section and obtained band time series
Extracted time series
count 0: 324 bands
count 1: 327 bands
count 2: 322 bands
Wavelet transform of the time series
wavelet scale [pixels]
10^0
10^1
10^2
section x axis [pixels]

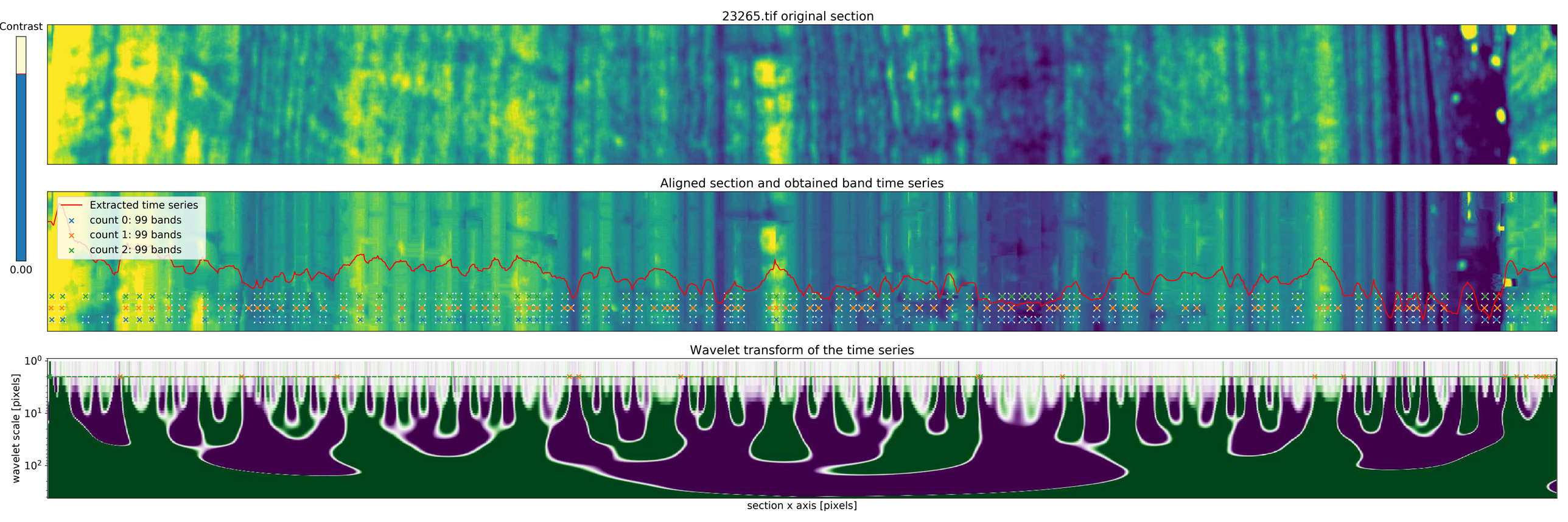
23265.tif original section
Contrast
0.00
Aligned section and obtained band time series
Extracted time series
count 0: 99 bands
count 1: 99 bands
count 2: 99 bands
Wavelet transform of the time series
10^0
10^1
10^2
wavelet scale [pixels]
section x axis [pixels]